

The properties of satellite galaxies in simulations of galaxy formation

Takashi Okamoto^{1,2*}, Carlos S. Frenk², Adrian Jenkins², Tom Theuns^{2,3}

¹ *Center for Computational Sciences, University of Tsukuba, 1-1-1 Tennodai, Tsukuba 305-8577 Ibaraki, Japan*

² *Institute for Computational Cosmology, Department of Physics, Durham University, South Road, Durham, DH1 3LE*

³ *Department of Physics, University of Antwerp, Campus Groenenborger, Groenenborgerlaan 171, B-2020 Antwerp, Belgium*

Accepted . Received ; in original form

ABSTRACT

We investigate the properties of satellite galaxies in cosmological N -body/SPH simulations of galaxy formation in Milky Way-sized haloes. Because of their shallow potential wells, satellite galaxies are very sensitive to heating processes which affect their gas content. Their properties can therefore be used to constrain the nature of feedback processes that regulate galaxy formation. In our simulations, we assume that all the energy produced by supernovae is used as kinetic energy to drive galactic winds. Several of our simulations produce bright, disc-dominated galaxies. We find that wind models in which the wind speed, v_w , is proportional to the local velocity dispersion of the dark matter, σ (and thus the wind mass-loading, $\eta_w \propto \sigma^{-2}$), make star formation in satellites sporadic, reproduce the observed satellite luminosity function reasonably well (down to $M_v = -7$) and match the luminosity-metallicity relation observed in the Local Group satellites. By contrast, models that assume a constant wind speed overproduce faint satellites and predict an incorrect luminosity-metallicity relation. Our simulations therefore suggest that the feedback processes that operate on the scale of satellite galaxies should generate galactic outflows whose mass-loading varies inversely with the depth of the potential.

Key words: methods: numerical – galaxies: evolution – galaxies: formation – cosmology: theory.

1 INTRODUCTION

The ‘ Λ -cold dark matter’ (Λ CDM) model is now broadly accepted as the standard paradigm in cosmology. This model completely specifies the initial conditions for the formation of cosmic structure, as well as the values of the cosmological parameters. Thus, in principle, it is possible to calculate the predicted evolution of objects of any kind, provided that the relevant astrophysical processes are understood. The complexity of these processes makes computer simulations the ideal tool to investigate the formation of structure in the Universe.

There is a long history of attempts to simulate the formation of spiral galaxies from Λ CDM initial conditions (e.g. Abadi et al. 2003a; Sommer-Larsen et al. 2003; Governato et al. 2004; Robertson et al. 2004; Okamoto et al. 2005; Governato et al. 2007; Ceverino & Klypin 2009; Scannapieco et al. 2009). Early on an ‘angular momentum problem’ was identified. In the Λ CDM model, galaxies are generally assembled by mergers.

As fragments merge, their angular momentum, which is primarily invested in their orbits, is transferred to the outer halo. Thus, if these fragments already carry within them the majority of the baryons which will make up the final galaxy, then these baryons will end up in a slowly rotating central spheroid rather than in a disc (Frenk et al. 1985). The likely solution to the problem was also identified early on: the baryons must be kept from cooling into the fragments, perhaps by some form of feedback, until the merging activity has subsided after which they can cool smoothly to form a disc (Navarro & Benz 1991; Navarro & White 1994; Navarro, Frenk, & White 1995).

The nature of the angular momentum problem and the key role of feedback were explicitly demonstrated by Okamoto et al. (2005) who simulated the formation of three galaxies – all in the same dark matter halo – assuming three different models of feedback powered by the energy liberated in supernovae (SNe). The resulting three galaxies spanned the whole range of morphological types, from a pure spheroid to a disc galaxy with bulge-to-total mass ratio of 0.5. Zavala et al. (2008) explored these galaxies further and showed how, when the feedback is not strong enough to pre-

* E-mail: tokamoto@ccs.tsukuba.ac.jp

vent gas cooling early on, a spheroid forms, whereas strong feedback can result in the formation of a disc by infall of gas which approximately conserves its angular momentum.

The physical processes that establish the feedback loops required for disc galaxies to form are poorly understood, but almost certainly involve SNe energy and perhaps also energy extracted from a central black hole (e.g. Di Matteo et al. 2005; Okamoto et al. 2005; Sijacki et al. 2007; Booth & Schaye 2009). These processes occur on scales which are many orders of magnitude below those that can be followed directly in galaxy simulations from Λ CDM initial conditions. They must therefore be treated as ‘sub-grid’ physics. A number of authors have attempted this kind of modelling using various recipes leading to a new generation of simulations which are producing increasingly realistic disc galaxies (Springel & Hernquist 2003a; Robertson et al. 2004; Okamoto et al. 2005; Stinson et al. 2006; Governato et al. 2007; Scannapieco et al. 2008; Ceverino & Klypin 2009).

Although a full physical understanding of how galactic feedback processes work seems a long way away, it is worth trying to identify or constrain the ‘macroscopic’ properties to which those processes must give rise for a galaxy simulation to be successful. Since it seems clear that much of the activity must take place early on, a promising approach is to investigate how different feedback models influence the properties of surviving fragments which appear today as satellites of the main galaxy. This is the approach we take in this paper: we focus on the luminosity function and metallicity of satellites and examine how these properties are affected by different models of feedback.

The properties of satellites are interesting in their own right. For example, their luminosity function has often been claimed to pose a major problem for the CDM model because the number of satellites seen around the Milky Way is several orders of magnitude smaller than the number of substructures that survive the collapse of galactic haloes in N -body simulations (Klypin et al. 1999; Moore et al. 1999). However, there are various feedback processes that could explain why only a tiny fraction of subhaloes manage to make stars. SN heating is clearly one of them (Benson et al. 2002, 2003); another is the photoionization of gas at early times, which suppresses gas cooling and raises the thermal pressure of the gas, preventing it from accreting onto small dark matter haloes (Babul & Rees 1992; Efstathiou 1992; Thoul & Weinberg 1996; Quinn, Katz, & Efstathiou 1996; Gnedin 2000; Okamoto, Gao, & Theuns 2008a).

These processes can be readily modelled using semi-analytic techniques and such studies have shown that indeed they greatly reduce the number of visible satellites (Bullock, Kravtsov, & Weinberg 2000; Benson et al. 2002; Somerville 2002; Li et al. 2009; Maccio’ et al. 2009). Some doubt has recently been cast on the validity of these important conclusion because both the early studies and the more recent, but similar ones by Li et al. (2009) and Maccio’ et al. (2009), were based on Gnedin’s (2000) filtering mass description of reionization which appears to overestimate significantly the suppression of galaxy formation (Hoefl et al. 2006; Okamoto et al. 2008a). Maccio’ et al. (2009), however, have shown that even with the weaker suppression advocated by Okamoto et al. (2008a), acceptable satellite luminosity functions can still be obtained.

Hydrodynamic simulations are well suited for studying complex processes such as reionization and SN feedback *ab initio*, with a minimum of simplifying assumptions. An earlier generation of galaxy simulations showed that at least the brightest satellite galaxies are produced in acceptable numbers (Governato et al. 2007; Libeskind et al. 2007). These simulations, however, lacked the numerical resolution required to study the bulk of the observed Milky Way satellites.

The simulations presented in this paper include a number of baryonic processes known to be relevant to galaxy formation. In particular, we model SN feedback as winds, a phenomenological approach which was originally introduced by Springel & Hernquist (2003a). Oppenheimer & Davé (2006) modified this treatment allowing the wind speed and mass-loading to vary with galaxy properties, while Okamoto et al. (2008b) introduced a model in which the energy in the winds reflects the timed-release of SN energy. Unlike in previous simulations, Dalla Vecchia & Schaye (2008) considered the case in which wind particles are allowed to interact hydrodynamically with interstellar medium (ISM) particles and found that due to hydrodynamical drag in the ISM, both the *effective* wind speed and the *effective* mass-loading (i.e. the wind speed and mass-loading when the wind leaves the star-forming region) change significantly from the *input* wind speed and mass-loading. This type of wind models are also used in recent cosmological simulations (e.g. Crain et al. 2009; Schaye et al. 2010).

Winds are now observed in many star-forming galaxies. Earlier data (Martin 1999; Heckman et al. 2000) suggested that their properties were independent of galactic properties. More recent observations (Martin 2005; Rupke, Veilleux, & Sanders 2005), however, have reversed this view: galaxies with higher circular velocity and higher star formation rates appear to drive faster winds. In this paper, we consider two types of wind models, both of which assume that all the energy released from SNe is converted into the kinetic energy of the winds. In one case, the wind speed is assumed to be constant, as in Springel & Hernquist (2003a) and as suggested by the earlier data (Martin 1999). In the other case, the wind speed is assumed to be proportional to the local velocity dispersion, as suggested by the more recent data (Martin 2005; Rupke et al. 2005). Similar, but different wind models have been used successfully to investigate the ejection of intergalactic metals (Oppenheimer & Davé 2006, 2008) and the galaxy mass-metallicity relation of massive galaxies ($M_* \gtrsim 10^9 M_\odot$; Finlator & Davé 2008).

This paper is organised as follows. In Section 2, we describe our simulations, providing brief descriptions of our modelling of baryonic processes (Section 2.1), the energetic and chemical feedback due to stellar evolution (Section 2.2) and the implementation of winds (Section 2.3). In Section 3 we present our results. We first focus on the properties of the central galaxies (Section 3.1). We then address how the luminosity functions and metallicities of the satellite galaxies are affected by different feedback prescriptions (Section 3.2). In Section 3.3 we perform convergence tests by using a higher resolution simulation. Finally, in Section 4, we discuss the results and summarise our main conclusions.

2 THE SIMULATIONS

We selected the three most massive objects from the sample of six Aquarius haloes described in Springel et al. (2008). The Aquarius haloes, extracted from a large cosmological simulation, were chosen to be relatively isolated and to have masses suitable to host a Milky Way-like galaxy. With one exception, which is not in our sample, they all have a relatively quiet merger history since $z = 1$. The three most massive haloes are: Aq-A, Aq-C, and Aq-D. Halo Aq-A has the quietest merger history of the whole sample and has been studied in the most detail to date. All our simulations follow galaxy formation within a periodic cube of side $100 h^{-1}$ Mpc in a Λ CDM cosmology with parameters: $\Omega_m = 0.25$, $\Omega_\Lambda = 0.75$, $\Omega_b = 0.045$, $\sigma_8 = 0.9$, $n_s = 1$, and $H_0 = 100 h \text{ km s}^{-1} \text{ Mpc}^{-1} = 73 \text{ km s}^{-1} \text{ Mpc}^{-1}$. These values are the same as those adopted for the Millennium Simulation (Springel et al. 2005) and the Aquarius project, and, within the uncertainties, are consistent with the current set of constraints from the WMAP 1-year (Spergel et al. 2003) and 5-year (Komatsu et al. 2009) data.

Hydrodynamic simulations of galaxy formation in all six Aquarius haloes have been presented by Scannapieco et al. (2009). These have similar resolution to our simulations but use a different code and focus on different issues. They employed a slightly lower value of the mean baryon density, $\Omega_b = 0.04$, than us. In that work, Aq-C, produced the most disc-dominated galaxy and had the smallest mass fraction in subhaloes within r_{50} (the radius inside which the density is fifty times the critical density). Aq-D has a similar halo mass to Aq-A and Aq-C¹. The concentration parameter of this halo is the smallest of the three we have chosen².

Since hydrodynamic simulations are much more computationally expensive than N -body simulations with the same number of dark matter particles, we are only able to simulate haloes at the lowest and next-to-lowest resolution employed in Springel et al. (2008) (corresponding to levels 5 and 4 in that paper). To test for numerical convergence, we carried out a high resolution simulation of Aq-D, to which we refer as Aq-D-HR (which corresponds to level 4). In Table 1, we summarise the halo properties, the particle masses and the gravitational softenings used for the simulations.

2.1 Baryonic processes

The simulation code was developed from an early version of GADGET-3. This is similar to the publicly available GADGET-2 (Springel 2005), but it has a more efficient load-balancing algorithm. We have modified GADGET-3 to follow a number of additional physical processes as follows.

Both photo-heating by a spatially uniform, time-evolving ultraviolet background and radiative cooling depend on gas metallicity, as described in Wiersma, Schaye, & Smith (2009a), by assuming the gas to be optically thin and in ionization equilibrium. We use the

ultraviolet background given by Haardt & Madau (2001) which is switched on at $z = 9$ (see also Okamoto et al. (2008a)). The cooling/heating routine described by Wiersma et al. (2009a) computes the cooling/heating rates individually for eleven elements whose contribution to the radiative cooling is significant (H, He, C, N, O, Ne, Mg, Si, S, Ca, and Fe). In the simulations, we track only nine elements and we take S and Ca to be proportional to Si (see Wiersma et al. 2009b).

As in Okamoto et al. (2005), we use the smoothed metallicity, rather than the particle metallicity (which is normally used), to compute the photo-heating and radiative cooling rates and to give the initial amount of each individual chemical element to newly-born stars. Wiersma et al. (2009b) found that the particle metallicity underestimates the metallicity of relatively unenriched gas compared to the smoothed value and thus significantly underpredicts the total stellar mass formed in their cosmological simulations. Using the particle metallicity is particularly problematic when a small fraction of metal enriched particles are ejected as winds, as in our simulations.

Star formation is modelled as in Okamoto et al. (2008b). That is, we treat an SPH particle whose density exceeds a threshold density for star formation ($n_H > n_{H,th} = 0.1 \text{ cc}^{-1}$) as a hybrid particle that contains two distinct phases: hot ambient gas and cold clouds, as in Springel & Hernquist (2003a). In this model, the clouds have a fixed mass spectrum and the star formation rate in a giant molecular cloud is a function of the ambient pressure according to the two-phase model of Samland & Gerhard (2003). Booth et al. (2007) introduced an alternative to the hybrid particle approach in which the cold clouds are represented by sticky particles (and hot, warm, and diffuse phases are represented by SPH particles). While this model shares many physical processes with our model, such as cloud formation by thermal instability and cooling and evaporation by thermal conduction, it allows the cloud mass spectrum to evolve with time through coagulation.

Stellar evolution is modelled as in Okamoto et al. (2008b), with two exceptions: (i) we employ the more realistic Chabrier initial mass function (IMF, Chabrier 2003), instead of the Salpeter IMF (Salpeter 1955); and (ii) we use metallicity-dependent stellar lifetimes and chemical yields (Portinari, Chiosi, & Bressan 1998; Marigo 2001). The code does not assume the instantaneous recycling approximation. The production of metals by SNe and AGB stars, stellar mass loss and SN feedback all take place on the timescale dictated by stellar evolution considerations. It is however important to note that published nucleosynthesis yields and stellar lifetimes vary significantly amongst authors. A detailed discussion of this topic may be found in Wiersma et al. (2009b). The stellar population synthesis model PÉGASE2 (Fioc & Rocca-Volmerange 1997) is used to calculate the luminosity of the simulated galaxies.

We now discuss the technical implementation of important “subgrid” processes included in our simulations.

2.2 Supernova energy and mass loss

In our simulations each star particle represents a simple stellar population (SSP), specified by its IMF, age, and metallicity. All stars more massive than $8M_\odot$ are assumed to explode

¹ Other Aquarius haloes have mass a factor of ~ 2 smaller than these haloes

² The values of the concentration parameter, c , for haloes Aq-A, Aq-C, and Aq-D, obtained by fitting an NFW density profile (Navarro, Frenk, & White 1997), are ~ 16 , 15 , and 9 , respectively (Springel et al. 2008).

as SNe II. As the simulation proceeds, the supernova energy, mass loss, and associated metals produced by a star particle are spread out over neighbouring particles. We use the lifetime and yields given by Portinari et al. (1998). While it would be most natural to distribute these quantities at each of the timesteps used to compute the dynamics, this proves to be prohibitively expensive computationally (particularly for SNe Ia). We adopt instead a more economical stochastic scheme, introduced by Okamoto et al. (2008b), in which the distribution operation takes place within a smaller number of discrete time intervals during the lifetime of an individual star particle.

From the time a star particle is born until it reaches the age, t_{8M_\odot} , corresponding to the lifetime of an $8M_\odot$ star, (~ 40 Myr for solar metallicity), the distribution of mass, metals and supernova energy to neighbouring particles occurs in a series of discrete events set by a timestep, Δt_{II} , of magnitude a fiftieth of t_{8M_\odot} . After an age t_{8M_\odot} there are no more SNe II, and a longer controlling timestep is introduced: $\Delta t_{Ia} = 100$ Myrs. This longer step is chosen specifically to follow SNe Ia, but it is also sufficiently small to allow the distribution of elements produced by AGB stars, as well as stellar mass loss from the SSP as a whole. In general, the dynamical timestep, Δt , is much shorter than either Δt_{II} or Δt_{Ia} . As a precaution, however, for star particles with an age less than t_{8M_\odot} , the dynamical time is explicitly limited to a maximum of half of Δt_{II} .

For a star particle with an age, $t < t_{8M_\odot}$, we define the conditional probability that the star particle undergoes a discrete event resulting in the distribution of energy, mass, and metals during a particular dynamical timestep, Δt , as follows:

$$\begin{aligned} p_{II} &= \frac{\int_t^{t+\Delta t} r_{II}(t') dt'}{\int_{t_0}^{t_0+\Delta t_{II}} r_{II}(t') dt' - \int_{t_0}^t r_{II}(t') dt'} \\ &= \frac{\int_t^{t+\Delta t} r_{II}(t') dt'}{\int_{t_0}^{t_0+\Delta t_{II}} r_{II}(t') dt'}, \end{aligned} \quad (1)$$

where $r_{II}(t)$ is the SN II rate for the SSP of age t and t_0 is the age when the previous SN II timestep finished. The SN II rate, $r_{II}(t)$, can be directly computed from the IMF, $\Phi(m) \equiv dN/dm$, and the stellar lifetime, $t(m)$ as

$$r_{II}(t) = -\Phi(m) \frac{dm(t)}{dt} \text{ for } t(m_u) \leq t \leq t_{8M_\odot}, \quad (2)$$

where the IMF is normalised as

$$\int_{m_u}^{m_l} m \Phi(m) dm = 1, \quad (3)$$

and m_u and m_l are the upper and lower limits of the IMF respectively. (We assume $m_u = 100 M_\odot$ and $m_l = 0.1 M_\odot$) The total number of SNe II produced by an SSP of $1 M_\odot$ is 1.18×10^{-2} . We generate a uniform random number between zero and one at every Δt . When p_{II} exceeds this number, the energy, mass, and metals expelled by the SSP during the interval t_0 to $t_0 + \Delta t_{II}$ are distributed over the neighbouring gas particles and the probability is set to zero until the end of this SN II timestep³.

The energy, metals and mass produced by a particle are

distributed amongst its 40 nearest neighbouring gas particles at each of these discrete events. It is important that each quantity that is being redistributed be accurately conserved. To ensure that this happens, the fraction of each quantity received by the i -th gas particle neighbouring the star is given by $m_i / \sum_j m_j$, where the subscript j runs over all 40 neighbours. We find that the results are relatively insensitive to the exact number of neighbours, with 32–128 particles producing similar behaviour.

The same procedure applies after an age t_{8M_\odot} , except that the timestep is now Δt_{Ia} . We calculate the SN Ia rate using the scheme of Greggio & Renzini (1983) with the updated parameters of Portinari et al. (1998). We take chemical yields and stellar mass loss from intermediate mass stars from Marigo (2001). Further details may be found in Okamoto et al. (2005), Nagashima et al. (2005) and references therein.

In summary, our method for treating feedback and mass loss allows us to perform the expensive neighbour search only once per star particle per SN timestep and results in the correct distribution of SNe in time, even with large SN timesteps, when averaged over many particles. Note that the method guarantees a single distribution event per star particle per SN timestep.

2.3 Galactic winds

In our subgrid model of feedback, SN explosions give rise to a wind by imparting kinetic energy to nearby gas particles. We assume that all of the energy released from SNe is potentially available to power the kinetic energy of the wind. Hence in terms of feedback efficiency, there is no difference among our models.

In order to prevent gas particles outside star-forming regions from being launched as winds⁴, we assume that only star-forming gas particles ($n_H > n_{H,th} = 0.1 \text{ cm}^{-3}$, where $n_{H,th}$ is the threshold density above which star formation can occur) are eligible to become wind particles. If low density gas particles ($n_H < n_{H,th}$) receive feedback energy, we simply add it to their internal energy.

During any given timestep, an eligible gas particle may receive supernova energy, ΔQ , from one or more neighbouring star particles. If this happens, then the particle is selected to become a wind particle during that timestep with a probability:

$$p_w = \frac{\Delta Q}{\frac{1}{2} m_{SPH} v_w^2}, \quad (4)$$

where m_{SPH} is the mass of the gas particle and v_w is the initial wind speed. The value of v_w is discussed later in this subsection. Having decided whether a particle is to become a wind particle or not, we set its value, $\Delta Q = 0$.

This procedure ensures that the kinetic energy is injected *locally* and that the generation of winds is consistent with the timed release of SN energy and metals. This is

³ Δt_{II} is $E_{SN} \int_{t_0}^{t_0+\Delta t_{II}} r_{II}(t') dt'$, where E_{SN} is the energy released by each supernova which, throughout this paper, we take to be $E_{SN} = 10^{51} \text{ erg}$

⁴ This can occur, for example, if a SN Ia is produced by a star in a low density gas environment.

³ For example, the energy released by an SSP of $1M_\odot$ during

an important difference from the widely used wind model of Springel & Hernquist (2003a) in which the wind particles are selected stochastically from all the star-forming gas (i.e. with $n_{\text{H}} > n_{\text{H,th}}$) in the simulation and are therefore not local to young star particles⁵. A different implementation of locally generated winds can be found in Dalla Vecchia & Schaye (2008).

It is possible for p_{w} to exceed unity. We deal with this situation using an iterative procedure. Firstly, the particle is added to the wind and we record both its label and the value of its ‘excess’ energy, $\Delta Q - \frac{1}{2}m_{\text{SPH}}v_{\text{w}}^2$. Having considered all eligible gas particles to decide which become wind particles, we then revisit those with excess energy and redistribute this energy to neighbouring non-wind gas particles. We then consider those particles whose density makes them eligible to be selected as a wind particle, recompute p_{w} including the reassigned excess energy from ΔQ in Eqn. 4, and decide whether they are converted into wind particles or not in the usual way. If there are still values of p_{w} which exceed unity, a further iteration is begun, and these iterations continue until there is no more excess energy to redistribute. In practise no more than two iterations are ever required.

When a particle is selected as a wind particle, its velocity, \mathbf{v} , is incremented as:

$$\mathbf{v}' = \mathbf{v} + v_{\text{w}}\hat{\mathbf{n}}. \quad (5)$$

The unit vector $\hat{\mathbf{n}}$ is chosen at random to be either parallel or anti-parallel to the vector $(\mathbf{v} - \bar{\mathbf{v}}) \times \mathbf{a}_{\text{grav}}$, where $\bar{\mathbf{v}}$ ideally would be chosen to be the velocity of the centre of mass of the galaxy. Since it is difficult to determine this velocity as the simulation proceeds, we instead select the average velocity of the neighbouring 40 dark matter particles as a proxy. The gravitational acceleration, \mathbf{a}_{grav} , on the other hand, includes contributions from matter everywhere in the simulation. In practise, for the central regions of haloes and subhaloes, both the magnitude and direction of \mathbf{a}_{grav} are largely determined by the local mass distribution. Adding a velocity according to Eqn. 5 leads to wind particles being ejected preferentially along the rotation axis of a spinning object, thus generating an ‘axial wind’ (Springel & Hernquist 2003a). Note that while the momentum is not strictly balanced when a single particle is placed in the wind, the momentum and angular momentum are statistically conserved because of the random orientation of the momentum kick along direction $\hat{\mathbf{n}}$.

Since the physical mechanisms that drive the outflows in galaxies are not well understood and the mass in winds is hardly constrained by observations, we adopt two phenomenological models for the properties of the winds (both of which assume that all of the supernova energy is available to power the outflows). The first model (which we label ‘vw’ for ‘variable wind’) assumes that the initial wind speed, v_{w} , is proportional to the one-dimensional velocity dispersion, σ , determined from the 40 neighbouring dark matter particles of the gas particle in question. That is, in the ‘vw’ model, $v_{\text{w}} \propto \sigma$, as suggested by recent data (Martin 2005).

Here, we are taking the local velocity dispersion as a proxy for the circular velocity. We have checked that the local velocity dispersion measured at the position of a star-forming gas particle is strongly correlated with the maximum of the circular velocity profile of its host (sub)halo, V_{max} , and that the relation between them ($V_{\text{max}} \simeq 1.45\sigma$) does not evolve with redshift.

In order to characterise the ‘vw’ models, we discuss wind properties by assuming the instantaneous recycling approximation and considering only SNe II as the energy source for the winds. While we do not make these assumptions in the simulations, considering this simplest of cases is instructive. With these assumptions, the energy ejection rate, \dot{E}_{SN} , is proportional to the star formation rate, \dot{M}_{\star} . Therefore, the mass flux in the winds in the ‘vw’ models, \dot{M}_{w} , can be written as:

$$\dot{M}_{\text{w}} = 2 \frac{\dot{E}_{\text{SN}}}{v_{\text{w}}^2} \propto \frac{\dot{M}_{\star}}{\sigma^2}, \quad (6)$$

because the wind speed, v_{w} , is proportional to the local dark matter velocity dispersion, σ . From these considerations, the wind mass-loading, η_{w} , can be expressed as:

$$\eta_{\text{w}} \equiv \frac{\dot{M}_{\text{w}}}{\dot{M}_{\star}} = \left(\frac{\sigma}{\sigma_0} \right)^{-2}, \quad (7)$$

where σ_0 is a parameter defined by the IMF and the feedback efficiency. We give the values of σ_0 in our models in Table 2. As mentioned earlier, we adopt the Chabrier IMF and make use of all the SN energy to power the kinetic energy of the winds.

For the second wind model (which we label ‘cw’ for ‘constant wind’), we assume a constant initial wind speed, which implies a constant mass-loading. This type of wind model has been widely used in hydrodynamic simulations of galaxy formation (e.g. Springel & Hernquist 2003a; Nagamine, Springel, & Hernquist 2004; Okamoto et al. 2008b).

In both the ‘vw’ and ‘cw’ models, we assume that newly launched wind particles are *decoupled* from hydrodynamical interactions for a brief period of time in order to enable the winds to emerge from a location close to the surface of their star-forming region with the *specified* wind velocity and mass-loading. This wind decoupling has been widely used in simulations since it was introduced by Springel & Hernquist (2003a).

Dalla Vecchia & Schaye (2008) compared *coupled* (i.e. not decoupled) and *decoupled* winds in detail and found that coupled winds blow bubbles and drive turbulence or create channels in the gas disc, while decoupled winds remove fuel for star formation without disturbing the gas disc. More importantly, for a given set of (input) wind speed and mass-loading, coupled winds are more efficient at suppressing star formation in low mass galaxies because they drag gas along; consequently the mass-loading when they leave the star-forming region (i.e. the effective mass-loading) is much larger than the input one. On the other hand, coupled winds are less efficient in high mass galaxies because they suffer large energy losses due to drag in the high-pressure ISM and the decelerated winds cannot escape from the galaxy (or often even from the star-forming region) (Schaye et al. 2010).

Since we wish to investigate the effects of two different feedback models on the population of satellite galaxies,

⁵ Note however that in Springel & Hernquist (2003a) the gas particle metallicity is updated according to its star formation rate; hence the non-local winds are consistent with the chemical enrichment scheme.

in which wind speed and mass-loading depend differently on the galaxy properties, we employ *decoupled* winds in this paper in order to specify the *effective* wind velocity and mass-loading as inputs. Full hydrodynamical interactions are enabled once a wind particle leaves the star-forming region ($n_{\text{H}} < 0.1n_{\text{H,th}}$) or after the time, $10 \text{ kpc}/v_{\text{w}}$, has elapsed, whichever occurs earlier⁶.

2.4 Models

For the variable wind models, we show results for $v_{\text{w}} = 5\sigma$ and $v_{\text{w}} = 4\sigma$; we refer to these as ‘vw5 σ ’ and ‘vw4 σ ’, respectively. Although we also calculated a model with $v_{\text{w}} = 3\sigma$, we do not show the results here because this wind speed is insufficient to allow gas particles to escape from their host halo and thus star formation is hardly suppressed compared to the no feedback case (Okamoto et al. 2008b).

For the constant wind models, we show results for $v_{\text{w}} = 700$ and 600 km s^{-1} ; we label them ‘cw700’ and ‘cw600’, respectively. We employ a slightly faster wind speed than was used in Okamoto et al. (2008b) ($v_{\text{w}} = 500 \text{ km s}^{-1}$) because we find that this wind speed is too low to suppress the early starbursts that would turn our galaxies into bulge-dominated objects (Okamoto et al. 2005). We believe that this is due to the fact that the baryon fraction in our current models is 35% higher than in the cosmological model adopted by Okamoto et al. (2008b). The values of the wind mass-loading factor, η_{w} , for these models are given in Table 2.

For the models introduced so far, we employ a multiphase model for the star-forming gas, as described in Okamoto et al. (2008b), in which a minimum pressure for star-forming gas, $P_{\text{min}} \propto \rho^{1.4}$, is imposed in order to stabilise gas discs against gravitational instability. Such a stiff equation of state for the star-forming gas was first introduced by Springel & Hernquist (2003a) in an attempt to allow for the fact that the interstellar medium (ISM) is supported by a hot gas phase which is unresolved in the simulations. On the other hand, Wada & Norman (2001, 2007) suggested that the multi-phase ISM is supported by turbulent motions induced by the self-gravity of the gas and galactic rotation. In any case, Robertson et al. (2004) argued that a stiff equation of state for the star-forming gas is required to form a disc. Our adoption of such an equation of state is intended to allow for these unresolved and ill-understood processes.

Artificial fragmentation of a disk may occur when simulations do not properly resolve the local Jeans length (Truelove et al. 1997; Bate & Burkert 1997). In order to prevent this from happening, several authors have adopted a similar strategy to us by imposing a minimum pressure for high-density gas (Robertson & Kravtsov 2008; Saitoh et al. 2008; Ceverino et al. 2009; Crain et al. 2009; Schaye et al. 2010).

Schaye et al. (2010) found that the global star formation rate is almost completely independent of both the equation of state of the ISM and the star formation law because the star formation is highly self-regulated by the winds. We therefore perform simulations without this multiphase

Table 2. Wind models and their properties. v_{w} and η_{w} denote the initial wind speed and the wind mass-loading (see text).

Model	v_{w} (km s^{-1})	η_{w}	Multiphase
vw5 σ_{single}	5σ	$\left(\frac{\sigma}{217 \text{ km s}^{-1}}\right)^{-2}$	No
vw5 σ	5σ	$\left(\frac{\sigma}{217 \text{ km s}^{-1}}\right)^{-2}$	Yes
vw4 σ	4σ	$\left(\frac{\sigma}{271 \text{ km s}^{-1}}\right)^{-2}$	Yes
cw700	700	2.4	Yes
cw600	600	3.3	Yes

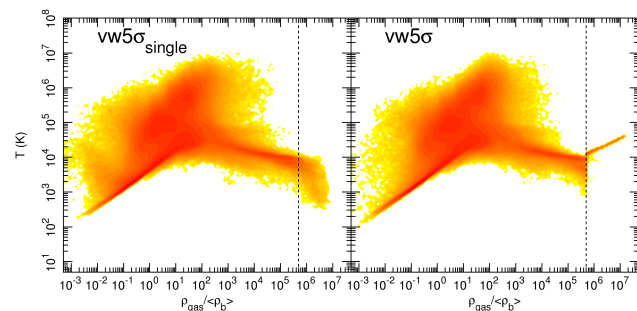


Figure 1. Distribution of gas particles in the density-temperature phase diagram for the Aq-A halo at $z = 0$. The left and right panels show the ‘vw5 σ_{single} ’ and ‘vw5 σ ’ models, respectively. The density above which star formation is enabled is indicated by the vertical dotted line. The ISM is well enriched by $z = 0$. As a result there is low-temperature ($< 10^4 \text{ K}$) star-forming gas in the ‘vw5 σ_{single} ’ model which has been cooled by metal-line cooling. We show the effective temperature for the multiphase star-forming gas in the ‘vw5 σ ’ model. Most of the star-forming gas lies on the line specified by $P_{\text{min}} \propto \rho^{1.4}$.

model for comparison. In this case, the star-forming gas can cool down to the equilibrium temperature set by the balance between photoheating and radiative cooling. Note that metal enriched gas can cool far below 10^4 K because we include metal-line cooling (Wiersma et al. 2009a). We use this single-phase gas in a ‘vw5 σ ’ wind simulation and label it ‘vw5 σ_{single} ’.

In Fig. 1 we compare the gas distribution in the density-temperature phase diagrams for the ‘vw5 σ_{single} ’ and ‘vw5 σ ’ simulations in the Aq-A halo at $z = 0$. Whereas the star-forming gas in the ‘vw5 σ_{single} ’ model cools down to $\sim 100 \text{ K}$ because of metal-line cooling and an increasing cooling rate with density, the gas in the ‘vw5 σ ’ model lies on the imposed minimum temperature. The equation of state of the star-forming gas in the ‘vw5 σ ’ model is hence much stiffer than that in the ‘vw5 σ_{single} ’ model. For both ISM models, the star formation efficiency is normalised to reproduce the observed relation between the surface star formation rate density and the surface gas density (Kennicutt 1998).

3 RESULTS

We begin this section by presenting an overview of the properties of the central galaxies. While our main focus is on the satellite galaxy population, the bulk properties

⁶ In our simulations, the first condition ($n_{\text{H}} < 0.1n_{\text{H,th}}$), is usually satisfied first.

Table 1. Numerical parameters relating to our four sets of initial conditions. The virial mass, M_{vir} , is defined as the mass within a sphere whose mean density is equal to the virial density at redshift zero computed from the spherical collapse model (Eke et al. 1996). The gravitational softening lengths, ϵ , are kept fixed in comoving coordinates for $z > 3$; thereafter they are frozen in physical units and to values presented in the table.

Halo	$M_{\text{vir}} (h^{-1} M_{\odot})$	$m_{\text{DM}} (h^{-1} M_{\odot})$	$m_{\text{SPH}} (h^{-1} M_{\odot})$	$\epsilon (h^{-1} \text{ kpc})$
Aq-A	1.4×10^{12}	1.9×10^6	4.1×10^5	0.425
Aq-C	1.2×10^{12}	1.5×10^6	3.4×10^5	0.425
Aq-D	1.3×10^{12}	1.9×10^6	4.1×10^5	0.425
Aq-D-HR	1.3×10^{12}	1.6×10^5	3.5×10^4	0.175

of the central galaxies, including their morphology, are a useful aid in understanding the nature of our wind models which, in turn, are the key to understanding the properties of the satellites (Maller & Dekel 2002; Okamoto et al. 2005; Zavala et al. 2008). A more detailed analysis of the central galaxies will be presented in a forthcoming paper.

3.1 The central galaxies

A visual impression of the structure of our simulated galaxies may be gained from Fig. 2 which shows edge-on views of the galaxies at $z = 0$. To make these images, we define a ‘ z ’ axis for each central galaxy as the direction of the angular momentum of all stars within $0.05R_{\text{vir}}$ of the centre at $z = 0$. We take R_{vir} to be the radius of a sphere that has the virial overdensity given by the spherical collapse model (Eke et al. 1996). We define two mutually perpendicular axes, ‘ x ’ and ‘ y ’, at random for each simulation, perpendicular to the z -axis. Fig. 2 shows that striking differences in the morphologies of the galaxies arise in each of the haloes Aq-A, Aq-C and Aq-D, when the wind prescription is varied. This supports the claim of Okamoto et al. (2005) that the morphology of simulated galaxies is very sensitive to the details of the physics implemented in the simulation. For example, for halo Aq-C a mere change of $\sim 15\%$ in the wind speed from 700 km s^{-1} to 600 km s^{-1} results in a change from a disc-dominated galaxy to a spheroidal galaxy. Nonetheless, it is encouraging that some models do successfully form disc-dominated galaxies.

The morphology of a galaxy is largely dictated by the angular momentum distribution of the stars. To quantify this, we analyse the distribution of the orbital circularity, defined below, of stars in the central galaxies. We exclude stars belonging to the satellites (which we define precisely in the next subsection). For each star belonging to a central galaxy we compute, J_z , the component of specific angular momentum parallel to the z -axis defined earlier. We then compute the specific angular momentum, $J_c(E)$, of a pro-grade circular orbit with the same binding energy as the particle. To evaluate $J_c(E)$, we first compute the circular velocity profile of the host halo, $v_c(r)$. The specific binding energy of a particle on a circular orbit at radius r is then given by

$$E(r) = -\frac{GM(<r)}{r} + \frac{1}{2}v_c(r)^2. \quad (8)$$

Similarly, the specific angular momentum of a particle at r is:

$$J_c(r) = rv_c(r). \quad (9)$$

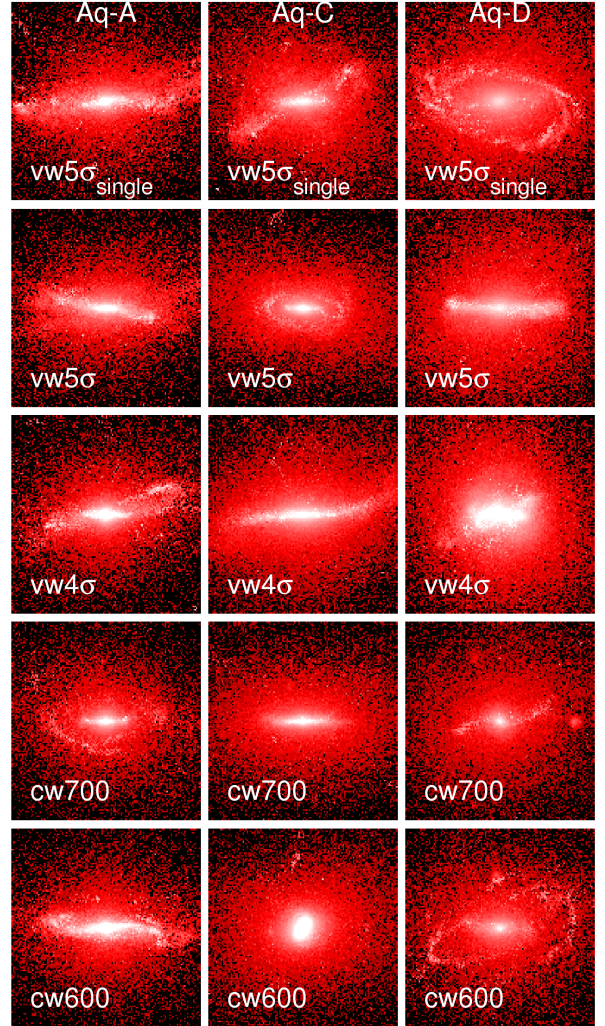


Figure 2. Edge-on views of the central galaxies at $z = 0$. The brightness is coded by the B -band surface brightness within a $50h^{-1} \text{ kpc}$ box centred on each galaxy. The viewing angles are determined using the angular momentum of stars within 5% of the virial radii of the host haloes. The Aq-A, Aq-C, and Aq-D haloes are shown from left to right, and models, ‘vw5 σ_{single} ’, ‘vw5 σ ’, ‘vw4 σ ’, ‘cw700’, and ‘cw600’ are shown from top to bottom.

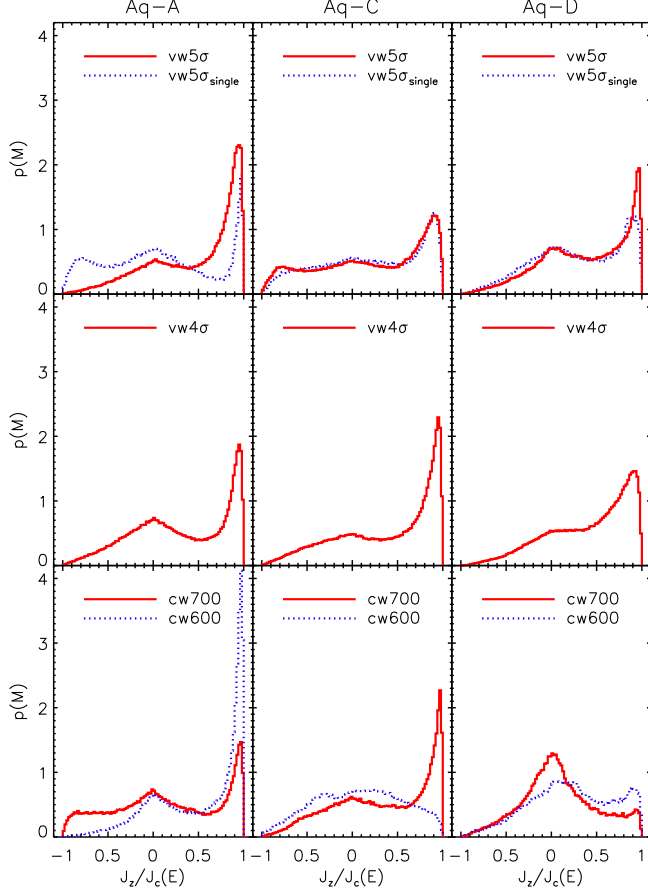


Figure 3. The mass-weighted normalised distribution of orbital circularity, $J_z/J_c(E)$, of all stars at $z = 0$ lying within R_{vir} of the centre, excluding stars identified as members of satellite galaxies. The Aq-A, Aq-C, and Aq-D haloes are shown from left to right and the ‘vw5 σ ’, ‘vw4 σ ’, and ‘cw’ models are shown from top to bottom. A peak at $J_z/J_c(E) \simeq 1$ indicates the existence of a disc component. The ‘vw5 σ_{single} ’ and ‘cw700’ models of the Aq-A halo and the ‘vw5 σ ’ model of the Aq-C halo exhibit a retrograde disc component as well as a prograde one.

We then calculate the specific energy of the i -th star particle assuming a spherically symmetric halo:

$$E_i = -\frac{GM(< r_i)}{r_i} + \frac{1}{2}v_i^2. \quad (10)$$

We identify the radius, r , of the circular orbit of specific binding energy, $E(r) = E_i$ using a Newton-Raphson method. This then gives the value of $J_c(E_i)$. The ratio $J_z/J_c(E)$ defines the orbital circularity (Abadi et al. 2003b; Okamoto et al. 2005).

Fig. 3 shows the normalised distribution of the orbital circularity of stars in the central galaxy within R_{vir} . A cold disc component has $J_z/J_c(E) \simeq 1$ and such a component is evident in most of the galaxies except in the ‘cw600’ model of the Aq-C halo. The ‘cw600’ model produces the most disc-dominated galaxy in the Aq-A halo, but the least disc-dominated galaxy in the Aq-C halo. For a fixed wind model, halo-to-halo differences in the final galaxy morphology reflect differences in the formation and merging histories of the haloes (even though most of them have similar quiet histories at early times). Galaxy morphology is particularly

sensitive to formation history in the ‘cw’ models because of the introduction of a critical velocity scale for the winds⁷. In the ‘vw’ case, the dependency on halo formation history is much weaker.

In Aq-A and Aq-D, the most pronounced discs among the ‘vw’ models form in the ‘vw5 σ ’ model, but in Aq-C, it is the ‘vw4 σ ’ which produces the largest disc. The ‘vw5 σ_{single} ’ galaxies are less disc-dominated than their ‘vw5 σ ’ counterparts. That confirms an earlier claim that the stiffer equation of state of the star-forming gas helps disc formation (Robertson et al. 2004). The effect is, however, not always evident (see Aq-C). Interestingly, the ‘vw5 σ_{single} ’ and ‘cw700’ models of the Aq-A halo and the ‘vw5 σ ’ model of the Aq-C halo exhibit counter-rotating or retrograde discs in addition to the prograde discs. The origin of these counter-rotating discs will be discussed in a forthcoming paper.

Our ‘vw’ galaxies are more disc-dominated than those simulated by Scannapieco et al. (2009) in the same Aquarius haloes, using very similar initial conditions but a different galaxy formation code. Since galaxy morphology is very sensitive to the details of feedback, this discrepancy is not surprising and probably reflects the fact that the strong feedback in the ‘vw’ models is able to suppress star formation in small haloes more efficiently than that in their simulations.

As emphasised by Okamoto et al. (2005), the star formation history of a galaxy is correlated with its morphology. Star formation histories for the central galaxies in our simulations are shown in Fig. 4. The ‘vw5 σ ’ and ‘vw5 σ_{single} ’ models are very similar, indicating that the star formation history is even less sensitive to the adopted ISM model than the morphology of the galaxy. This is consistent with the conclusions of Schaye et al. (2010) who find that the global star formation is highly self-regulated by feedback and is almost independent of the choices of equation of state for the ISM and star formation law.

The ‘vw5 σ ’ and ‘vw4 σ ’ models are also similar except that the ‘vw4 σ ’ model for the Aq-D halo has significantly higher star formation rate at low redshift. It is interesting that the ‘cw600’ model of the Aq-C halo has a relatively high star formation rate at low redshift, a feature which was claimed to be a sign of disc formation (Okamoto et al. 2005), although in this case this galaxy is dominated by a spheroidal component (see Fig. 2 and 3). Note that our sample of Aquarius haloes all have quiet merger histories at low redshift. As recently stressed by Scannapieco et al. (2009), the origin of galaxy morphology is more complicated than we generally thought and the star formation history is only a very crude indicator of the final morphology.

3.2 The satellite galaxies

We now turn to an investigation of how different feedback models affect the properties of satellites. We identify subhaloes using the SUBFIND algorithm (Springel et al. 2001) and restrict attention to subhaloes of at least 32 particles. In counting the number of particles in a subhalo, we include not only dark matter but also baryonic particles. Therefore it is,

⁷ This is not true for coupled winds (see Dalla Vecchia & Schaye 2008).

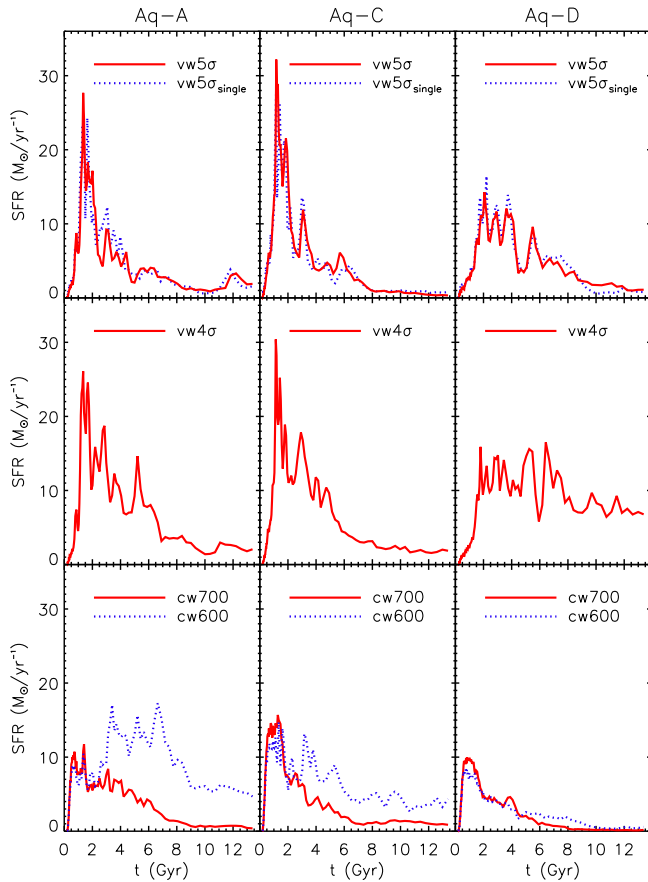


Figure 4. The star formation histories of the central galaxies. Only stars within $0.1R_{\text{vir}}$ of the central galaxy which are not members of a satellite galaxies are shown. The panels and lines are the same as in Fig. 3. The ‘vw5 σ_{single} ’ and ‘vw5 σ ’ models show almost identical star formation histories, implying that the modelling of the ISM has little effect on the star formation histories and that it is the wind model which is the most important ingredient in determining the morphology of the galaxy.

in principle, possible to identify purely baryonic gravitationally bound objects. We define satellite galaxies as subhaloes that contain at least 10 star particles. In Sec. 3.3 we check the robustness of this definition and carry out a convergence test.

3.2.1 The satellite luminosity function

In Fig. 5, we plot the satellite luminosity functions in our simulations and compare them with observations of the Local Group. The observed luminosity function of bright ($M_V < -11$) satellites lying within 280 kpc of either the Milky Way or M31 is constructed from the data compiled by Metz, Kroupa, & Jerjen (2007). The data of Koposov et al. 2008, which includes the incompleteness-corrected SDSS ultrafaint satellites within 280 kpc from the centre of the Milky Way, are represented by a power-law. The host galaxy haloes, defined by the friends-of-friends algorithm (Davis et al. 1985), extend beyond 280 kpc, but, for consistency with the observations, in constructing the luminosity functions we consider only the satellites within 280 kpc of

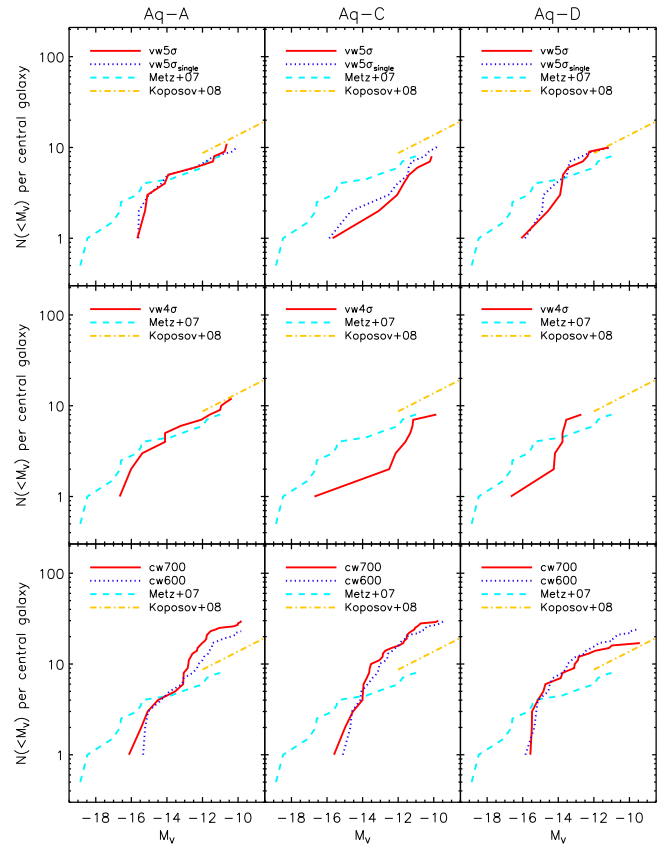


Figure 5. Satellite luminosity functions. Only satellites within 280 kpc from the central galaxies are counted. The panels are the same as in Fig. 3. The solid lines show the results from the simulations. The dashed line shows the luminosity function for the bright ($M_V < -11$) Milky Way and M31 satellites, similarly taking only those within 280 kpc from either galaxy, constructed from the data compiled by Metz et al. (2007). The dot-dashed line is a power-law fit to the luminosity function of Koposov et al. (2008) which includes newly discovered SDSS ultra-faint satellites, again restricted to include only satellites within 280 kpc of the Milky Way.

the centre. For other analyses below we will make use of larger samples of satellites.

For a given wind model, the satellite luminosity function varies significantly from halo to halo, reflecting the variation in the number of massive subhaloes (Springel et al. 2008; Ishiyama et al. 2009). This alerts us to the danger of assuming that the Milky Way is a typical galaxy. The ‘vw5 σ_{single} ’ and ‘vw5 σ ’ models again yield almost identical results. Interestingly, the ‘cw700’ and ‘cw600’ models also produce results almost indistinguishable from each other. The ‘vw5 σ ’ and ‘vw4 σ ’ models are similar except that the brightest satellite in a ‘vw4 σ ’ model is slightly brighter than its counterpart in the corresponding ‘vw5 σ ’ model reflecting the lower wind speed in the former model.

Our results are consistent with the conclusion of the semi-analytic study by Benson et al. (2002) that it is difficult to form satellite galaxies as bright as the LMC in Milky Way-sized haloes. Although in the ‘vw4 σ ’ model for the ‘Aq-D’ halo there is a nearby galaxy as bright as M33, it does not qualify as a satellite galaxy according to our strict defi-

dition which requires satellites to be within a radius of 280 kpc from the central galaxy.

Away from the bright-end, the ‘vw’ models (in which the wind mass-loading increases towards smaller subhaloes) do reproduce the observed satellite luminosity function reasonably well. By contrast, both of the ‘cw’ models have overly steep luminosity functions with too many faint satellites. The constant mass-loading wind model is not able to suppress star formation in these faint satellites sufficiently. We expect that if we had adopted the momentum-driven wind model favoured by Oppenheimer & Davé (2006, 2008), in which the wind mass-loading, η_w , is proportional to σ^{-1} , we would have obtained satellite luminosity functions whose faint-end slopes are steeper than those in our ‘vw’ models ($\eta_w \propto \sigma^{-2}$). On the other hand, it seems likely that if we had not assumed that the winds are decoupled for a short period time, the faint end of the resulting luminosity functions in the ‘cw’ cases would have been shallower than in our decoupled ‘cw’ models (Dalla Vecchia & Schaye 2008; Schaye et al. 2010). Within any given halo, the ‘vw’ models always match the satellite luminosity function better than the ‘cw’ models. From this point of view there is little to choose between the ‘vw5 σ ’ and ‘vw4 σ ’ versions.

The robustness of our results depends on how well the low-mass end of the subhalo mass function is resolved in the simulations. In order to identify the smallest resolved subhalo, we first compute the cumulative subhalo abundance as a function of maximum subhalo circular velocity, $N(> V_{\max})$. We then fit this cumulative velocity function with a power-law, $N(> V_{\max}) \propto V_{\max}^\alpha$; subhalo velocity functions in N-body simulations are well represented by a power-law with $\alpha \sim -3$ (e.g. Diemand et al. 2007; Springel et al. 2008).

We define the smallest resolved circular velocity as the V_{\max} value at which the velocity function first deviates by 10% from the power-law fit. We have computed this for the ‘vw5 σ ’ and ‘cw700’ models of the Aq-D halo, which is the halo we use for convergence tests later. For the ‘vw5 σ ’ model we find a value of 12.9 km s^{-1} , which is consistent with the V_{\max} at which the subhalo velocity function begins to deviate from that of the high-resolution counterpart (Aq-D-HR). The smallest V_{\max} of the subhaloes which contain at least 10 star particles (i.e. the satellites) is 22.8 km s^{-1} . We conclude that the subhaloes that host satellites in the ‘vw’ models are well resolved. For the ‘cw700’ model, the minimum resolved circular velocity is 11.2 km s^{-1} , which is consistent with the value for the vw5 σ model. However, now the smallest V_{\max} of the satellites is 13.2 km s^{-1} , which is close to the resolution limit. Thus, in the ‘cw’ models, the flattening seen at the very faint end of the luminosity functions could be affected by numerical limitations.

3.2.2 Metallicity and abundance patterns

We now investigate the metallicity of satellites which, in principle, is also a sensitive diagnostic of the feedback physics (e.g. Arimoto & Yoshii 1987; Finlator & Davé 2008). In Fig. 6, we plot the iron abundance as a function of satellite luminosity. (To compare our simulations with the data, we adopt the values for the solar abundances given

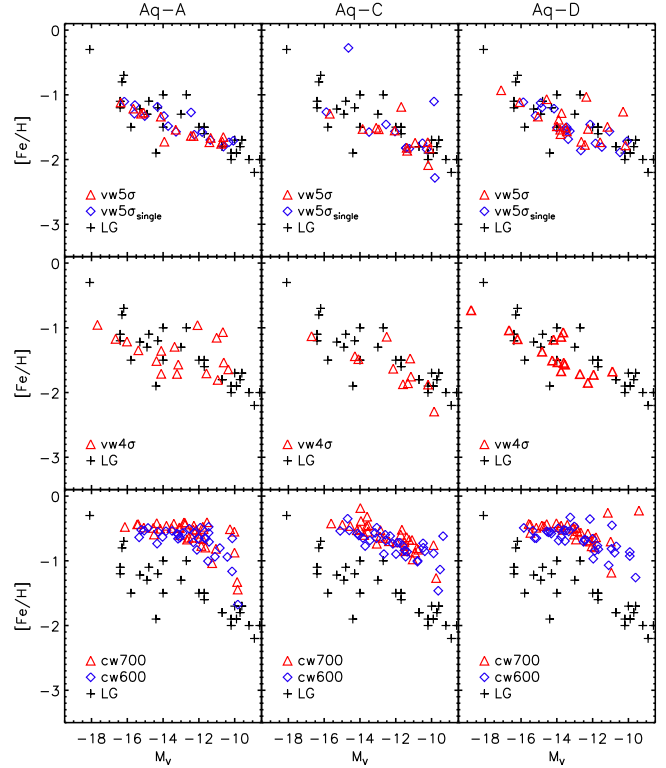


Figure 6. The iron abundance relative to solar for satellite galaxies, as a function of the absolute V -band magnitude. The panels are the same as in Fig. 3. The abundances for the Local Group satellites are taken from Mateo (1998), with the exception of the Magellanic Clouds which was taken from Hill et al. (1995). Different symbols correspond to different wind models as indicated in the legend. The Local Group data are shown by plus signs.

by Grevesse & Sauval (1998)⁸. All of the ‘vw’ models reproduce the observed luminosity-metallicity relation for the Local Group satellites quite well. On the other hand, the iron abundance of the ‘cw’ satellites is almost a constant function of the satellite luminosity, reflecting the constant wind mass-loading factor. These results strongly support models in which the wind mass-loading scales as $\eta_w \propto \sigma^{-2}$. A momentum-driven wind would most likely produce a relation intermediate between those of the ‘vw’ and ‘cw’ models, thus too shallow to match the data, while a coupled wind model would like produce a steeper relation than the corresponding ‘cw’ and ‘vw’ models.

The alpha element-to-iron abundance ratio is often used as a measure of the star formation timescale (e.g. Nagashima & Okamoto 2006). Since SNe Ia hardly produce alpha elements, $[\text{O}/\text{Fe}]$ decreases with time if a star formation episode lasts longer than $\sim 1 \text{ Gyr}$, which is a typical SNe Ia timescale. For an SSP of solar metallicity, it takes $\sim 0.9 \text{ Gyr}$ for SNe Ia to produce as much iron as that produced by SNe II⁹. In Fig. 7, we show the oxygen-

⁸ Assuming the more recent values for the solar abundances given by Asplund et al. (2005) increases $[\text{Fe}/\text{H}]$ in the simulations only by ~ 0.16 .

⁹ Assuming solar metallicity, the first SN Ia goes off at $t \sim 75 \text{ Myr}$ in our model.

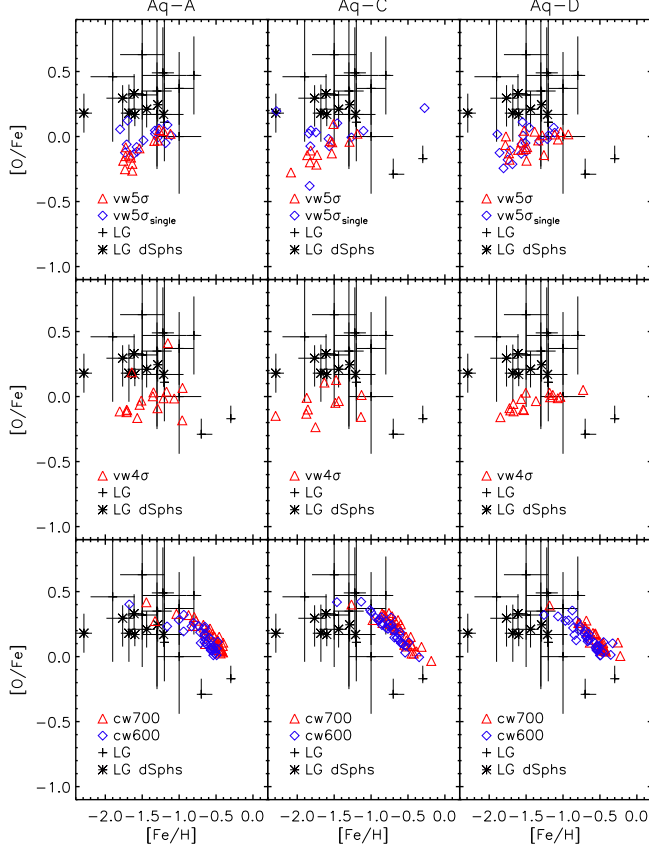


Figure 7. The oxygen-to-iron abundance ratio of satellite galaxies as a function of the iron abundance. The panels correspond with those in Fig. 6. In addition to data from the sources given in Fig. 6, we plot the median values for Local Group dwarf spheroidal taken from Shetrone, Côté, & Sargent (2001) and Shetrone et al. (2003). For Mateo’s data, the error bars represent 1σ error, while for the Magellanic Clouds and dwarf spheroidal they show the larger of the 25-75 percentile interval or the observational 1σ error.

to-iron abundance ratio of satellite galaxies¹⁰ as a function of their iron abundance. Most of the satellites in the ‘vw’ models have $[O/Fe] \sim 0$, which is slightly lower than the observed values. This might imply that the star formation timescales in the simulated dwarf satellites are too long, or that the model employed for the SN Ia is incorrect (e.g. Kobayashi et al. 1998; our SN Ia rate was calculated using the scheme described by Greggio & Renzini 1983, with parameters updated according to Portinari et al. 1998), or that the assumed IMF is inaccurate (e.g. Nagashima et al. 2005). Both the SN Ia rate and the nucleosynthesis yields are highly uncertain (see e.g. Wiersma et al. 2009b). Exploring these issues is, however, beyond the scope of this paper and we defer this to future work.

The ‘cw’ models reproduce the observed abundance patterns in the Milky Way satellites reasonably well, even

though they fail to match their iron abundance (see Fig. 6). The reasons behind the different patterns in the ‘vw’ and ‘cw’ are instructive. In the ‘vw’ models, the wind mass-loading is larger for smaller galaxies resulting in more metal poor dwarfs (see Fig. 6); this, in turn, suppresses star formation. However, the wind speed, $v_w \sim 4\text{--}5\sigma$, allows expelled gas to fall back later (see Oppenheimer & Davé 2008), thus lengthening the effective star formation timescale. In the ‘cw’ models, there is a critical velocity at which the wind speed is equal to the escape velocity from the halo, v_{esc} . For $v_w \gg v_{\text{esc}}$, the gas blown out of a halo never comes back and therefore the winds shorten the effective star formation timescale. As a result, galaxies with small V_{max} become alpha-enhanced. When the wind speed is of the order of the escape velocity, the expelled gas is recycled as a fountain. Hence, when $v_w \lesssim v_{\text{esc}}$, the effective star formation timescale is longer than when $v_w \gg v_{\text{esc}}$ and the oxygen-to-iron ratio begins to decrease relative to the value set purely by SNe II.

3.2.3 Star formation histories

The star formation histories of randomly selected satellites in two models, ‘vw5σ’ and ‘cw700’ in the Aq-D halo, are shown in panels (a) and (b) of Fig. 8, respectively. (We have checked that the other models of each type are similar to these.) These plots allow us to investigate how reionization and infall into a larger halo affect star formation. The arrows indicate the ‘accretion’ redshift, i.e. the moment when the main progenitor of a satellite actually becomes a satellite galaxy by falling into a larger halo. The labels give the maximum of the circular velocity of the selected satellites, V_{max} , in km s^{-1} , at $z = 0$.

We find that reionization (which happens at $z_{\text{re}} = 9$) has little impact on the star formation histories of today’s satellites. Even the smallest of them continue to make stars past this epoch. As shown by Okamoto & Frenk (2009), however, this is not the case for haloes that are too small at the epoch of reionization to host satellites. Haloes which have $V_{\text{max}} \lesssim 12 \text{ km s}^{-1}$ at the epoch of reionization are unable to hold on to their gas which is evaporated by the UV photons and thus end up as dark subhaloes today.

The figure shows that infall into a larger halo is important although it does not always immediately truncate star formation (see also Font et al. 2008). Okamoto & Frenk (2009) demonstrate that infall tends to strip gas off the infalling small object, eventually choking its star formation. A decrease in star formation soon after infall is apparent in some of the examples in the figure, such as the haloes with $v_c^{\text{max}} = 41.6, 39.2, 28.5, 23.8 \text{ km s}^{-1}$ shown in panel (a) for ‘vw5σ’. In a few cases, e.g. $v_c^{\text{max}} = 40.7, 31.4, 25.3 \text{ km s}^{-1}$, star formation does cease completely upon infall.

Similar remarks can be made regarding the satellites in the ‘cw700’ model. In this case, because the wind mass-loading is smaller than in the ‘vw’ models, subhaloes of smaller circular velocity can host satellites. The truncation of star formation at the time of accretion is more evident in satellites with such small circular velocities. As may be seen by comparing panel (a) and (b) of Fig. 8, at a given V_{max} , the star formation timescale is shorter in the ‘cw700’ model than in the ‘vw5σ’ model. In addition, the star formation in the ‘vw5σ’ model is more variable in time than in the ‘cw700’ model. These differences arise from the fact that a

¹⁰ Again, using more recent solar abundance determinations decreases $[O/Fe]$ in the simulations by 0.17. However, the data in Mateo (1998) assume $12 + \log(O/H)_{\odot} = 8.93$, which is consistent with the values given by Grevesse & Sauval (1998)

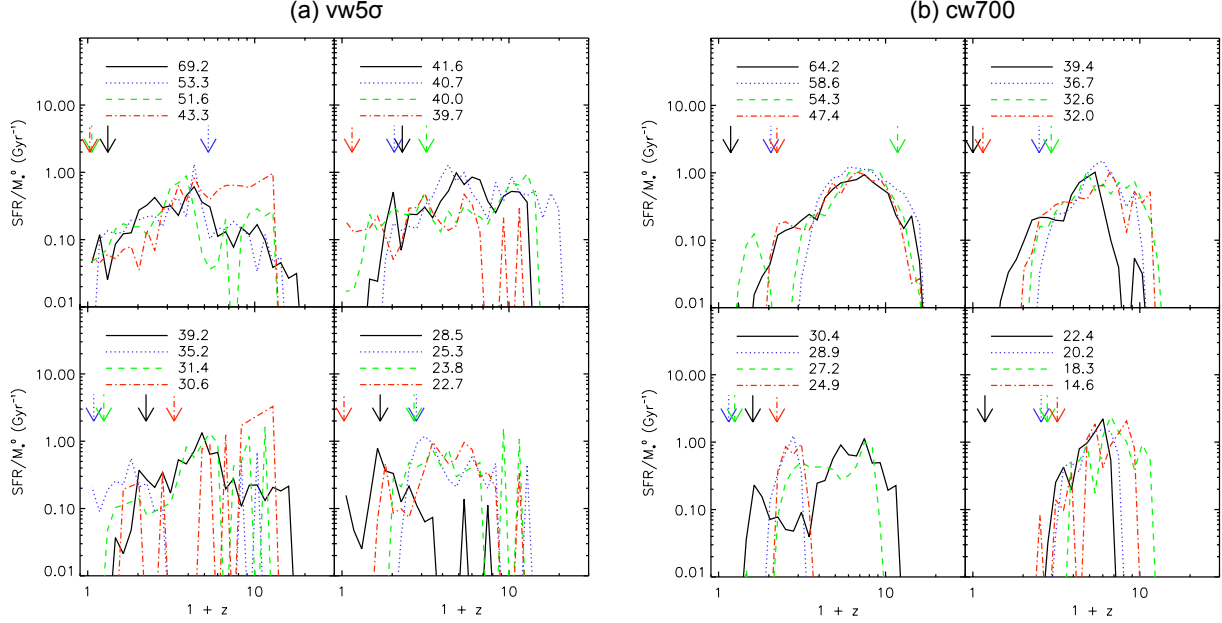


Figure 8. (a): The star formation rate divided by M_*^0 , the stellar mass at $z = 0$, for a selection of satellite galaxies in the 'vw5σ' model of the Aq-D halo. The labels give the value of V_{max} of each of the individual satellites, in km s^{-1} . The arrows indicate the redshift when the progenitors are accreted into a larger halo (i.e. when they become satellites). Note that we assume reionization occurs at $1 + z_{\text{re}} = 10$. (b): As (a) but for the 'cw700' model of the Aq-D halo.

wind speed of $v_w = 4 - 5\sigma$ in the 'vw' models can cause wind particles to escape from a halo which, however, can be re-accreted later on. By contrast, in the constant wind speed model, re-accretion is inhibited whenever $v_{\text{esc}} \ll v_w$ while a wind is suppressed whenever $v_{\text{esc}} > v_w$. As a result, the star formation timescale is shorter than in the 'vw' models whether $v_{\text{esc}} \ll v_w$ or $v_{\text{esc}} > v_w$. These differences in star formation histories explain the differences in abundance patterns seen between the two types of models (Fig. 7).

3.3 A high resolution simulation

In this subsection, we select the most promising wind model and investigate its sensitivity to numerical resolution by resimulating it with ten times higher mass resolution. We selected the 'vw5σ' model on the grounds that it provides the best overall match to the observed luminosity function and iron abundances of Local Group satellites (although the oxygen-to-iron ratios, which are sensitive to the adopted SN Ia rate, are systematically low). The run, Aq-D-HR, is detailed in Table 1 (thanks to its low concentration, the Aq-D halo is the least computationally expensive of the three). Since we only consider the 'vw5σ' model in this subsection, for simplicity, we refer to the high and low resolution simulations as Aq-D-HR and Aq-D (or simply as the high and low resolution simulations), respectively.

We first examine the correspondence between the positions of individual satellites in the two simulations. To do this, we trace the dark matter particles of a particular subhalo in one of the simulations back to the initial conditions and search for a matched subhalo in the other simulation (see Springel et al. 2008). We include all the satellites lying within 280 kpc in the low resolution simulation and the satellites in the high resolution simulation which also lie within

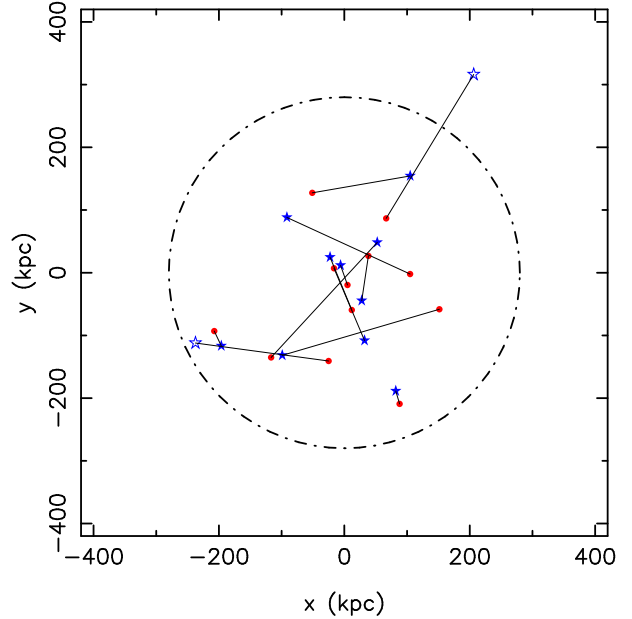


Figure 9. The projected positions of the matched satellites in the two simulations with different resolution, Aq-D-HR and Aq-D. The matching was carried out for satellites lying within 280 kpc from the centre that are brighter than $M_V = -11.2$, corresponding to the luminosity of the faintest satellite within 280 kpc in the lower resolution simulation. Matched pairs are joined by thin lines. Circles denote satellites in Aq-D-HR and stars in Aq-D; open symbols indicate satellites found outside the 280 kpc sphere which is marked by the dot-dashed line.

280 kpc and are brighter than $M_V = -11.2$, corresponding to the faintest luminosity of satellites within 280 kpc in the low resolution simulation.

The result is shown in Fig. 9, where the matched pairs are linked by a line. The mean spatial offset between matched pairs is ~ 100 kpc, somewhat larger than the mean offset of ~ 54 kpc found between matched pairs in Aq-A-4 and Aq-A-1¹¹ (Springel et al. 2008). This difference is not due to small number statistics - we have only 12 pairs of satellites - since a similar offset is found for matched pairs of all subhaloes within 280 kpc, whether or not they host satellites. The mismatch is more likely due to slight orbital phase deviations - which translate into large spatial separations - produced by differences in the potential of the two galaxies whose evolution is not identical, as we will show in Fig. 10. Slight difference in the mass of the subhaloes due to baryonic processes may also contribute to this offset. In spite of the relatively large spatial offsets, the photometric and chemical properties of the satellite populations in the two simulations are remarkably similar, as we will show later in this subsection.

In Fig. 10, we present the results of the convergence tests. We first compare the star formation histories in the central galaxies in two simulations in the upper-left panel. Although the shape of the two curves is very similar, the higher resolution simulation has a slightly lower mean star formation rate. This likely reflects enhanced mass loss through winds from small haloes not resolved in the lower resolution simulation. At $z = 0$, the stellar mass in the central galaxy is 18% lower in the Aq-D-HR simulation than in the Aq-D simulation.

The upper-right panel shows the satellite luminosity functions obtained in the two simulations. They agree very well. The slight differences between them arise mainly from the requirement that the samples should contain only satellites found within 280 kpc of the central galaxy. Two of the satellites in the high resolution simulation have counterparts in the low resolution simulation which lie outside the 280 kpc radius. One of these can be clearly seen in Fig. 9; the other one is projected inside the circle. When we include these two satellites, the luminosity functions in the low and high resolution simulations agree even better, down to the faintest satellite luminosity in the Aq-D ($M_V \simeq -11$). This suggests that our definition of satellites is robust. Encouragingly, the faint end of the satellite luminosity function in the high resolution simulation matches that of the newly discovered SDSS satellites (Koposov et al. 2008) remarkably well. This provides further support for the ‘vw’ winds in which $v_w \propto \sigma$ and $\eta_w \propto \sigma^{-2}$.

We again estimate the minimum resolved circular velocity of the subhaloes in the high-resolution simulation as described in Section 3.2.1. The minimum resolved value is 6.1 km s^{-1} , while the minimum value of the subhaloes that host a satellite is 12.1 km s^{-1} . Hence, all the subhaloes hosting satellites are well resolved in the simulation. The minimum V_{max} of the satellites in these models is set by reionization (Okamoto et al. 2008a; Okamoto & Frenk 2009).

In the lower panels of Fig. 10, we compare the chemical

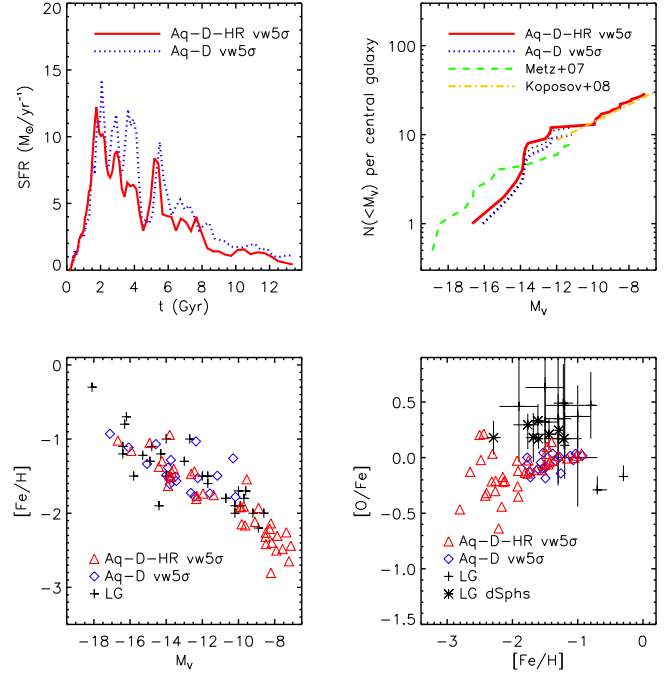


Figure 10. Comparison of the low and high resolution simulations of the ‘vw5σ’ model in the Aq-D halo. In all panels, the high resolution (Aq-D-HR) case is shown by solid lines and the low resolution (Aq-D) case by dotted lines. *Upper-left:* star formation histories of the central galaxies, as in Fig. 4. *Upper-right:* the satellite luminosity functions within 280 kpc, as in Fig. 5. The thin black dotted line shows the luminosity function of the low-resolution satellites that are matched to the bright ($M_V \geq -11.2$) high-resolution satellites. *Lower-left:* the iron abundance as a function of satellite luminosity, as in Fig. 6. *Lower-right:* oxygen-to-iron abundance as a function of the satellite luminosity, as in Fig. 7.

properties of the satellites in the two simulations. Both the iron abundance and the oxygen-to-iron ratios are consistent at the two resolutions. The high resolution simulation predicts that the luminosity-metallicity relation for satellites should extend down to at least $M_V \sim -7$ (lower-left panel). There is a hint in the lower-right panel that the oxygen-to-iron abundance ratio in the simulated satellites increases slightly with metallicity. This trend is possibly inconsistent with the Local Group dwarf spheroidal data, in which the alpha-to-iron abundance ratios appear to be almost constant or slightly increasing with decreasing metallicity (e.g. Tolstoy et al. 2009).

Comparing matched pairs individually, we find that the stellar mass in the high-resolution satellites is, on average, 30% higher than in their low-resolution counterparts. (This trend is opposite to that for the central galaxy where the high-resolution simulation forms a less massive galaxy.) The metallicity in the high-resolution satellites is, on average, only 8% higher than in the low-resolution simulation.

Finally, in Fig. 11, we show the star formation histories of a selection of satellites in the high-resolution simulation. The top and middle panels show the star formation histories of the matched counterparts shown in panels (a) of Fig. 8. These histories are qualitatively similar to those seen in the low resolution simulation (Fig. 8), indicating that

¹¹ Aq-A-4 has similar resolution to Aq-D-HR and Aq-A-1 has ~ 100 times better resolution than Aq-D-HR.

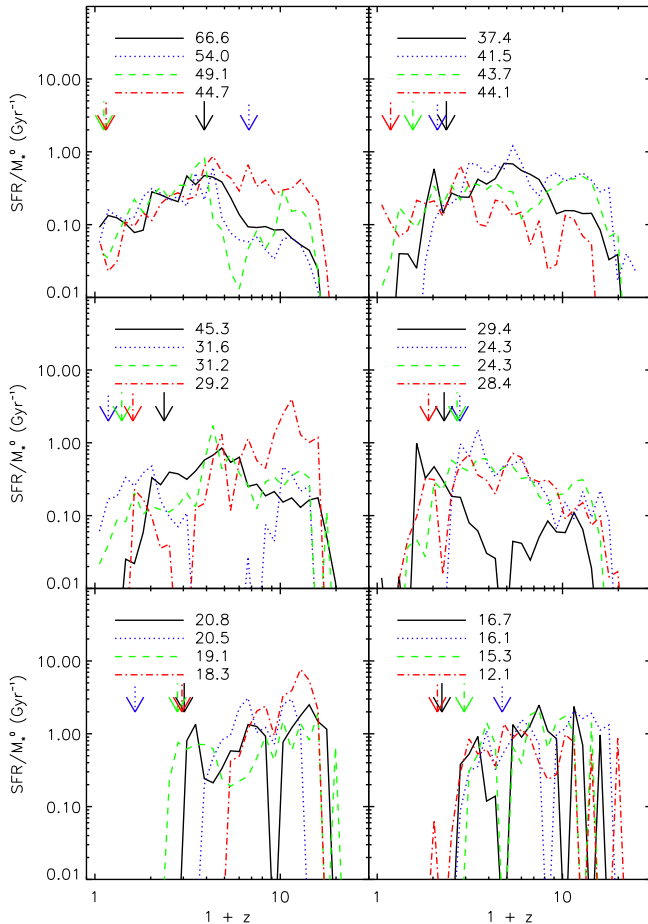


Figure 11. As (a) of Fig. 8, but for the ‘vw5 σ ’ model in the Aq-D-HR halo. The top and middle panels show star formation histories of matched high-resolution counterparts of the low-resolution satellites shown in (a) of Fig. 8. The bottom panels show star formation histories of satellites that are not resolved in Aq-D.

the time variability is not a resolution effect but a result of the winds. The sporadic nature of the star formation makes the effective star formation timescale longer (and lowers the alpha-to-iron ratio) in the ‘vw’ models compared to the ‘cw’ models. As we saw earlier, the star formation histories of the surviving satellites retain no obvious imprint of reionization. Even the satellites in the bottom panels of Fig. 11, which were not resolved in the low-resolution counterpart (Aq-D), continue forming stars past the reionization epoch. We note, however, that the gas content in subhaloes that has failed to form stars was evaporated at the epoch of reionization (Okamoto & Frenk 2009). This process is likely to be responsible for the suppression of cosmic star formation rate at the epoch of reionization found by larger cosmological simulations (Crain et al. 2009; Schaye et al. 2010). It is interesting to note that star formation in these smallest satellites ($V_{\text{max}} \lesssim 20 \text{ km s}^{-1}$) ceases at the time of accretion or earlier. We discuss in detail these sorts of effects on surviving satellites and failed satellites (i.e. subhaloes that do not host stars) in a companion paper (Okamoto & Frenk 2009).

In summary, our high resolution resimulation of the ‘vw5 σ ’ model shows that the statistical properties of the

satellite population in our low resolution calculations are robust to a change in mass resolution of a factor of ten. Furthermore, the high resolution simulation allows us to extend the model luminosity function by 4 magnitudes, thus enabling a comparison with recent data.

4 SUMMARY AND DISCUSSION

We have performed cosmological hydro-chemodynamic simulations of galaxy formation in 3 Milky Way-sized haloes taken from the Aquarius project (Springel et al. 2008). A primary aim of our study has been to constrain the nature of some of the feedback processes that must have operated during galaxy formation. We have done this by focusing on satellite galaxies whose shallow potential wells make them particularly sensitive to feedback effects. As a byproduct, we have been able to explore some of the controversial properties of satellite galaxies, such as their luminosity function, in the context of the Λ CDM cosmology which we have assumed in our simulations.

Although our simulations are amongst the largest of their kind performed to date, they lack the resolution to follow the physics of the interstellar medium directly. Such processes must be included as ‘sub-grid physics’. In particular, we have assumed that energy injected by SNe generate galactic winds. We have assumed further that all the energy released by SNe is deposited as kinetic energy in the winds.

Early studies, as well as more recent ones have shown that many observed galaxy properties cannot be reproduced unless most of the SN energy is used to blow gas out of galaxies (e.g. Springel & Hernquist 2003b; Okamoto et al. 2005; Oppenheimer & Davé 2008; Crain et al. 2009; Schaye et al. 2010). Since a large fraction of SN energy must be radiated away, other sources of energy seem to be required to power strong winds such as radiation from young stars (Murray et al. 2005; Nath & Silk 2009). In this study we have included these unresolved processes in a purely phenomenological way by assuming two types of ‘energy-conserving’ winds. In the first type, the initial wind speed is taken to be proportional to the local velocity dispersion of the dark matter, $v_w \propto \sigma$, as suggested by recent data (Martin 2005), and thus, the wind mass-loading, $\eta_w \propto \sigma^{-2}$ (‘vw’ models). In the second type, the initial wind speed and the wind mass-loading are assumed to be constant for all galaxies (‘cw’ models), as suggested by earlier data (Martin 1999). Disc-dominated galaxies formed in several of our simulations.

In some of our simulations, we included a multiphase model for star-forming gas, but we found that this made little difference to the outcome (see also Schaye et al. 2010), apart from the overall morphology of the central galaxy. The use of a stiff equation of state for the ISM tends to promote the formation of disc-dominated galaxies by stabilising gaseous discs against gravitational instability. The key to the diversity of behaviours that we find is not the treatment of the ISM, but rather the treatment of the SN-driven winds.

The ‘vw’ models give a reasonable match to the observed luminosity function of Local Group satellites. A major factor in this success is the behaviour of the mass-loading in the wind which becomes increasingly large in smaller

galaxies. If the mass-loading is kept constant as in the ‘cw’ case, galaxy formation is not sufficiently suppressed in small haloes resulting in a satellite luminosity function which rises much too steeply at the faint end. Previous SPH simulations had already shown that an acceptable match to the abundance of bright satellites can be obtained from Λ CDM initial conditions (Libeskind et al. 2007; Governato et al. 2007; Maccio’ et al. 2009), thus confirming the conclusion from early semi-analytic studies that the so-called ‘satellite problem’ in the CDM cosmology (Klypin et al. 1999; Moore et al. 1999) disappears when proper account is taken of the baryonic processes involved in galaxy formation (Bullock et al. 2000; Benson et al. 2002; Somerville 2002). Our high-resolution simulation, however, extends the comparison with the luminosity function to much fainter magnitudes than previous SPH simulations.

The ‘vw’ feedback model that produces an acceptable satellite luminosity function, also produces an acceptable luminosity-metallicity relation for the satellites. By contrast, the ‘cw’ model fails to reproduce this relation for the same reasons that it fails to reproduce the luminosity function: the constant mass-loading leads to an iron abundance in satellites with $v_{\text{esc}} \gg v_w$ which is essentially independent of luminosity, contrary to what is observed.

None of our ‘vw’ models reproduces the oxygen-to-iron abundance ratio measured for dwarf satellites. There are several possible reasons for this discrepancy: the star formation timescale may be too long, the model of SNe Ia or the IMF that we have adopted may be incorrect, or our assumed oxygen yield may be too low. Given the large uncertainties in the value of the yield, the IMF and SNe Ia rates, we do not consider this shortcoming of our models to be fatal although further work is required. For example, a top-heavy IMF in these metal-poor objects could provide the solution although it is unclear whether such a radical assumption would destroy the agreement of the model with other observables.

Based on our estimate of the minimum resolved circular velocity of subhaloes in the simulations, we find that subhaloes hosting satellites in the ‘vw’ models are reliably resolved down to the faintest magnitude. Thus, the faint-end slope of the satellite luminosity function and the luminosity-metallicity relation in the ‘vw’ models are robust. This conclusion is confirmed by a direct convergence study of one model (‘vw5 σ ’ of the Aq-D): low- and high-resolution simulations give consistent results. On the other hand, in the ‘cw’ models in which the smaller wind mass-loading factor allows satellites to form in halos with small values of V_{max} , the faint-end slope of the satellite luminosity function could be affected by limited numerical resolution although we estimate that any such effects would be restricted to the extreme faint end.

Barring the alpha-to-iron ratio, we conclude that an energy-conserving wind model in which the mass loading scales inversely with square of velocity dispersion provides a viable model for feedback as judged by the properties of satellite galaxies. Our preferred wind model is different from the ‘momentum-driven’ wind models favoured by Finlator & Davé (2008) in order to explain the mass-metallicity relation of large galaxies. In this kind of model, the wind speed is proportional to σ as in our ‘vw’ models, but the mass-loading scales as $\eta_w \propto \sigma^{-1}$ (rather than

as $\eta_w \propto \sigma^{-2}$). It could be that the mechanisms that drive galactic outflows in small and large galaxies are different.

In ‘vw’ models with wind speed, $v_w \simeq 4 - 5\sigma$, the mass loading is large in small galaxies. Winds therefore remove substantial amounts of star-forming gas, but much of this material eventually falls back onto the galaxy. As a result, the star formation in small satellites is episodic and has a much longer timescale than in the ‘cw’ models in which the gas is expelled from the small halo, never to return. These general properties underlie the different predictions for the number density of faint galaxies and their chemical properties in the different models.

The star formation histories of the satellites retain no obvious imprint of the reionization of gas at early times. Accretion onto larger haloes, on the other hand, often affects subsequent star formation and, in low mass satellites ($V_{\text{max}} \lesssim 20 \text{ km s}^{-1}$), it truncates it altogether. Only 5% of subhaloes whose circular velocities are higher than the minimum resolved value ($V_{\text{max}} > 6.1 \text{ km s}^{-1}$) in the high-resolution simulation (Aq-D-HR) host satellites. The vast majority of subhaloes do not manage to make a visible galaxy and remain dark. The mechanisms that distinguish visible from dark satellites are investigated in a companion paper (Okamoto & Frenk 2009).

ACKNOWLEDGEMENTS

We are grateful to Volker Springel for providing us with the GADGET-3 code and to Joop Schaye, Claudio Dalla Vecchia, and Rob Wiersma for providing us with tabulated radiative cooling and heating rates. Our simulations were performed at the Center for Computational Sciences in the University of Tsukuba, the Cosmology Machine at the ICC, Durham, and the Cray XT4 at CfCA of NAOJ. This work was supported in part by the *FIRST* project based on Grants-in-Aid for Specially Promoted Research by MEXT (16002003), Grant-in-Aid for Scientific Research (S) by JSPS (20224002), and an STFC rolling grant to the ICC. TO acknowledges financial support by Grant-in-Aid for Young Scientists (start-up: 21840015). CSF acknowledges a Royal Society Wolfson research merit award.

REFERENCES

- Abadi M. G., Navarro J. F., Steinmetz M., Eke V. R., 2003a, *ApJ*, 591, 499
- , 2003b, *ApJ*, 597, 21
- Arimoto N., Yoshii Y., 1987, *A&A*, 173, 23
- Asplund M., Grevesse N., Sauval A. J., 2005, in *Astronomical Society of the Pacific Conference Series*, Vol. 336, *Cosmic Abundances as Records of Stellar Evolution and Nucleosynthesis*, Barnes III T. G., Bash F. N., eds., p. 25
- Babul A., Rees M. J., 1992, *MNRAS*, 255, 346
- Bate M. R., Burkert A., 1997, *MNRAS*, 288, 1060
- Benson A. J., Bower R. G., Frenk C. S., Lacey C. G., Baugh C. M., Cole S., 2003, *ApJ*, 599, 38
- Benson A. J., Frenk C. S., Lacey C. G., Baugh C. M., Cole S., 2002, *MNRAS*, 333, 177
- Booth C. M., Schaye J., 2009, *ArXiv e-prints*

- Booth C. M., Theuns T., Okamoto T., 2007, *MNRAS*, 376, 1588
- Bullock J. S., Kravtsov A. V., Weinberg D. H., 2000, *ApJ*, 539, 517
- Ceverino D., Dekel A., Bournaud F., 2009, *ArXiv e-prints*
- Ceverino D., Klypin A., 2009, *ApJ*, 695, 292
- Chabrier G., 2003, *PASP*, 115, 763
- Crain R. A., Theuns T., Dalla Vecchia C., Eke V. R., Frenk C. S., Jenkins A., Kay S. T., Peacock J. A., Pearce F. R., Schaye J., Springel V., Thomas P. A., White S. D. M., Wiersma R. P. C., 2009, *MNRAS*, 399, 1773
- Dalla Vecchia C., Schaye J., 2008, *MNRAS*, 387, 1431
- Davis M., Efstathiou G., Frenk C. S., White S. D. M., 1985, *ApJ*, 292, 371
- Di Matteo T., Springel V., Hernquist L., 2005, *Nat*, 433, 604
- Diemand J., Kuhlen M., Madau P., 2007, *ApJ*, 667, 859
- Efstathiou G., 1992, *MNRAS*, 256, 43P
- Eke V. R., Cole S., Frenk C. S., 1996, *MNRAS*, 282, 263
- Finlator K., Davé R., 2008, *MNRAS*, 385, 2181
- Fioc M., Rocca-Volmerange B., 1997, *A&A*, 326, 950
- Font A. S., Johnston K. V., Ferguson A. M. N., Bullock J. S., Robertson B. E., Tumlinson J., Guhathakurta P., 2008, *ApJ*, 673, 215
- Frenk C. S., White S. D. M., Efstathiou G., Davis M., 1985, *Nat*, 317, 595
- Gnedin N. Y., 2000, *ApJ*, 542, 535
- Governato F., Mayer L., Wadsley J., Gardner J. P., Willman B., Hayashi E., Quinn T., Stadel J., Lake G., 2004, *ApJ*, 607, 688
- Governato F., Willman B., Mayer L., Brooks A., Stinson G., Valenzuela O., Wadsley J., Quinn T., 2007, *MNRAS*, 374, 1479
- Greggio L., Renzini A., 1983, *A&A*, 118, 217
- Grevesse N., Sauval A. J., 1998, *Space Science Reviews*, 85, 161
- Haardt F., Madau P., 2001, in *Clusters of Galaxies and the High Redshift Universe Observed in X-rays*, Neumann D. M., Tran J. T. V., eds.
- Heckman T. M., Lehnert M. D., Strickland D. K., Armus L., 2000, *ApJS*, 129, 493
- Hill V., Andrievsky S., Spite M., 1995, *A&A*, 293, 347
- Hoeft M., Yepes G., Gottlöber S., Springel V., 2006, *MNRAS*, 371, 401
- Ishiyama T., Fukushima T., Makino J., 2009, *ApJ*, 696, 2115
- Kennicutt Jr. R. C., 1998, *ApJ*, 498, 541
- Klypin A., Kravtsov A. V., Valenzuela O., Prada F., 1999, *ApJ*, 522, 82
- Kobayashi C., Tsujimoto T., Nomoto K., Hachisu I., Kato M., 1998, *ApJL*, 503, L155
- Komatsu E., Dunkley J., Nolte M. R., Bennett C. L., Gold B., Hinshaw G., Jarosik N., Larson D., Limon M., Page L., Spergel D. N., Halpern M., Hill R. S., Kogut A., Meyer S. S., Tucker G. S., Weiland J. L., Wollack E., Wright E. L., 2009, *ApJS*, 180, 330
- Koposov S., Belokurov V., Evans N. W., Hewett P. C., Irwin M. J., Gilmore G., Zucker D. B., Rix H.-W., Fellhauer M., Bell E. F., Glushkova E. V., 2008, *ApJ*, 686, 279
- Li Y.-S., Helmi A., De Lucia G., Stoehr F., 2009, *MNRAS*, 397, L87
- Libeskind N. I., Cole S., Frenk C. S., Okamoto T., Jenkins A., 2007, *MNRAS*, 374, 16
- Maccio' A. V., Kang X., Fontanot F., Somerville R. S., Koposov S. E., Monaco P., 2009, *ArXiv e-prints*
- Maller A. H., Dekel A., 2002, *MNRAS*, 335, 487
- Marigo P., 2001, *A&A*, 370, 194
- Martin C. L., 1999, *ApJ*, 513, 156
- , 2005, *ApJ*, 621, 227
- Mateo M. L., 1998, *ARA&A*, 36, 435
- Metz M., Kroupa P., Jerjen H., 2007, *MNRAS*, 374, 1125
- Moore B., Ghigna S., Governato F., Lake G., Quinn T., Stadel J., Tozzi P., 1999, *ApJL*, 524, L19
- Murray N., Quataert E., Thompson T. A., 2005, *ApJ*, 618, 569
- Nagamine K., Springel V., Hernquist L., 2004, *MNRAS*, 348, 421
- Nagashima M., Lacey C. G., Baugh C. M., Frenk C. S., Cole S., 2005, *MNRAS*, 358, 1247
- Nagashima M., Okamoto T., 2006, *ApJ*, 643, 863
- Nath B. B., Silk J., 2009, *MNRAS*, 396, L90
- Navarro J. F., Benz W., 1991, *ApJ*, 380, 320
- Navarro J. F., Frenk C. S., White S. D. M., 1995, *MNRAS*, 275, 56
- , 1997, *ApJ*, 490, 493
- Navarro J. F., White S. D. M., 1994, *MNRAS*, 267, 401
- Okamoto T., Eke V. R., Frenk C. S., Jenkins A., 2005, *MNRAS*, 363, 1299
- Okamoto T., Frenk C. S., 2009, *MNRAS*, 399, L174
- Okamoto T., Gao L., Theuns T., 2008a, *MNRAS*, 390, 920
- Okamoto T., Nemmen R. S., Bower R. G., 2008b, *MNRAS*, 385, 161
- Oppenheimer B. D., Davé R., 2006, *MNRAS*, 373, 1265
- , 2008, *MNRAS*, 387, 577
- Portinari L., Chiosi C., Bressan A., 1998, *A&A*, 334, 505
- Quinn T., Katz N., Efstathiou G., 1996, *MNRAS*, 278, L49
- Robertson B., Yoshida N., Springel V., Hernquist L., 2004, *ApJ*, 606, 32
- Robertson B. E., Kravtsov A. V., 2008, *ApJ*, 680, 1083
- Rupke D. S., Veilleux S., Sanders D. B., 2005, *ApJS*, 160, 115
- Saitoh T. R., Daisaka H., Kokubo E., Makino J., Okamoto T., Tomisaka K., Wada K., Yoshida N., 2008, *PASJ*, 60, 667
- Salpeter E. E., 1955, *ApJ*, 121, 161
- Samland M., Gerhard O. E., 2003, *A&A*, 399, 961
- Scannapieco C., Tissera P. B., White S. D. M., Springel V., 2008, *MNRAS*, 389, 1137
- Scannapieco C., White S. D. M., Springel V., Tissera P. B., 2009, *MNRAS*, 396, 696
- Schaye J., Dalla Vecchia C., Booth C. M., Wiersma R. P. C., Theuns T., Haas M. R., Bertone S., Duffy A. R., McCarthy I. G., van de Voort F., 2010, *MNRAS*, 402, 1536
- Shetrone M., Venn K. A., Tolstoy E., Primas F., Hill V., Kaufer A., 2003, *AJ*, 125, 684
- Shetrone M. D., Côté P., Sargent W. L. W., 2001, *ApJ*, 548, 592
- Sijacki D., Springel V., di Matteo T., Hernquist L., 2007, *MNRAS*, 380, 877
- Somerville R. S., 2002, *ApJL*, 572, L23
- Sommer-Larsen J., Götz M., Portinari L., 2003, *ApJ*, 596, 47
- Spergel D. N., Verde L., Peiris H. V., Komatsu E., Nolte M. R., Bennett C. L., Halpern M., Hinshaw G., Jarosik N.,

- Kogut A., Limon M., Meyer S. S., Page L., Tucker G. S., Weiland J. L., Wollack E., Wright E. L., 2003, *ApJS*, 148, 175
- Springel V., 2005, *MNRAS*, 364, 1105
- Springel V., Hernquist L., 2003a, *MNRAS*, 339, 289
- , 2003b, *MNRAS*, 339, 312
- Springel V., Wang J., Vogelsberger M., Ludlow A., Jenkins A., Helmi A., Navarro J. F., Frenk C. S., White S. D. M., 2008, *MNRAS*, 391, 1685
- Springel V., White S. D. M., Jenkins A., Frenk C. S., Yoshida N., Gao L., Navarro J., Thacker R., Croton D., Helly J., Peacock J. A., Cole S., Thomas P., Couchman H., Evrard A., Colberg J., Pearce F., 2005, *Nat*, 435, 629
- Springel V., White S. D. M., Tormen G., Kauffmann G., 2001, *MNRAS*, 328, 726
- Stinson G., Seth A., Katz N., Wadsley J., Governato F., Quinn T., 2006, *MNRAS*, 373, 1074
- Thoul A. A., Weinberg D. H., 1996, *ApJ*, 465, 608
- Tolstoy E., Hill V., Tosi M., 2009, *ArXiv e-prints*
- Truelove J. K., Klein R. I., McKee C. F., Holliman II J. H., Howell L. H., Greenough J. A., 1997, *ApJL*, 489, L179
- Wada K., Norman C. A., 2001, *ApJ*, 547, 172
- , 2007, *ApJ*, 660, 276
- Wiersma R. P. C., Schaye J., Smith B. D., 2009a, *MNRAS*, 393, 99
- Wiersma R. P. C., Schaye J., Theuns T., Dalla Vecchia C., Tornatore L., 2009b, *MNRAS*, 399, 574
- Zavala J., Okamoto T., Frenk C. S., 2008, *MNRAS*, 387, 364